energies

MDPI

Article

Correlational Analytical Characterization of Energy Dissipation-Liberation and Acoustic Emission during Coal and Rock Fracture Inducing by Underground Coal Excavation

Pengfei Shan *, Xingping Lai and Xiaoming Liu

School of Energy and Mining Engineering, Xi'an University of Science and Technology, Xi'an 710054, China; laixp@xust.edu.cn (X.L.); liuxiaoming@stu.xust.edu.cn (X.L.)

* Correspondence: shanpengfei@xust.edu.cn; Tel.: +86-1377-2190-561

Received: 4 April 2019; Accepted: 12 June 2019; Published: 20 June 2019

Abstract: This paper uses an acoustic emission (AE) test to examine the energy dissipation and liberation of coal and rock fracture due to underground coal excavation. Many dynamic failure events are frequently observed due to underground coal excavation. To establish the quantitative relationship between the dissipated energy and AE energy parameters, the coal and rock fracturing characteristics were clearly observed. A testing method to analyze the stage traits and energy release mechanism from damage to fracture of the unloading coal and rock under uniaxial compressive loading is presented. The research results showed that the relevant mechanical parameter discreteness was too large because the internal structures of the coal and rock were divided into multiple structural units (MSU) by a few main cracks. The AE test was categorized into four stages based on both the axial stress and AE event parameters: initial loading stage, elastic stage, micro-fracturing stage, and post-peak fracturing stage. The coal and rock samples exhibited minimum (maximum) U values of 60.44 J (106.41 J) and 321.19 J (820.87 J), respectively. A theoretical model of the dissipation energy during sample fracturing based on the AE event energy parameters was offered. The U decreased following an increase in $\Sigma E_{AE\text{-}II}/\Sigma E_{AE}$.

Keywords: Coal excavation; coal and rock fracture; multiple structural units (MSU); energy dissipation; AE energy

1. Introduction

An increasing number of coal mines exhibit deep-excavation status and require consideration attention due to the presence of mining problems that must be dealt with for increasing underground coal excavation depth increment [1]. More dynamic failure events, including rock burst in both the tunneling process and coal extraction, coal and gas outbursts, and mining-induced earthquakes, frequently occur and require the accurate prediction of all impending dynamic hazards [2]. A large number of engineering tests and experiments have indicated that coal fracture involves a sequence of micro- and macro-scale events, including initial crack deformation and propagation as well as macroscopic crack formation and propagation [3]. In addition, the dynamic failure of the coal is closely related to the mechanical mechanism of the coal under the mining unloading condition. Given the complexity of rock mechanics, research on the dynamic failure should emphasize energy concentration, storage, dissipation, and liberation. Many scholars have characterized the energy dissipation and liberation rules of void coal fracture using external loading. Zhao [4] proposed the minimum energy principle of the dynamic damage of the rock and indicated that authentic energy consumption during the dynamic failure was equal to the failure energy under the uniaxial stress status. Xie [5] indicated

that rock deformation and damage combined the energy dissipation and liberation results. Xie also indicated the strength loss criterion based on the energy dissipation and the global failure criterion based on releasable strain energy. According to the dissipated energy by cyclic loading, Jin [6] offered a theoretical calculation equation for the damage variable and the determination of the damage threshold from the perspective of the material damage variable defined by the energy dissipation. Li [7] applied damage to the rock crushing stage and used a fatigue damage iterative relational expression under the action of stress waves to the rock post-destruction stage to generate a quantitative relationship between the impact energy, rock damage, and fragmentation distribution. Li [8] established the energy identification criterion of the mesoscopic rock failure by using the strain energy density theory. The criterion was also applied in the failure simulation of the Brazil split test and intermediate crack tensile test.

Previous research [9,10] has led to remarkable achievements in three aspects: (i) establishing the relationship between the rock unit damage and energy dissipation from a microscopic perspective; (ii) determining the rock constitutive relation based on energy dissipation; and (iii) understanding the failure and fracturing of the rock based on the releasable strain energy. However, few experimental studies on the quantitative rules of energy dissipation and the liberation of the coal and rock have accounted for the excavation conditions have been conducted.

As a specific monitoring method, the acoustic emission (AE) method [11–16] has obvious advantages in studying both the damage-fracturing characteristics and energy dissipation-liberation of the coal and rock under complex the excavation conditions. Tang [17] established a hypothesis and a frame of a numerical simulation based on the rock AE regularity, and offered the distribution of the temporal-spatial sequence. With the deep rock burst process simulation system, He [18] examined the AE waveform and frequency traits of limestone rock burst under the true triaxial unloading condition. Feng [19] investigated the chemical erosion characteristics of rock fracturing in various rock AE tests with different stress settings, the results of which revealed the mechanisms of the rock physical-mechanical properties and crack propagation at different stress settings and chemical circumstances. Ji [20] offered the AE signal frequency characteristics under various rock-fracturing stages based on granite uniaxial compressed testing. By using a AE monitoring system, Zhao [21] studied the granite failure with prefabricated cracks under uniaxial compressed loading, thereby quantitatively establishing the three-dimensional evolution model of the internal microcrack and the regularity of the AE events with respect to both the loading time and its values.

Previous related research focused on AE regularity during rock fracturing under diverse loading conditions, the Kaiser effect theory, and the AE application. From the perspective of macroscopic energy conservation, however, a correlation must be established between the energy dissipation of the coal and rock, and the accumulated values of the periodical acoustic wave energy during the coal and rock fracturing to generate a mechanical mechanism on the degree of coal and rock fracturing.

In this paper, an AE test was developed to examine energy dissipation and liberation of coal and rock fracture under complex excavation conditions to generate a quantitative regularity between the dissipated energy of the coal and rock and the AE energy parameters. This regularity would not only characterize the coal and rock fracturing characteristics, but also would uncover the catastrophic mechanism of coal and rock fracturing. The results can provide a theoretical basis for the design and construction of rock engineering excavation in deep well circumstances.

2. Test Scheme

2.1. Crustal Stress Setting and Physical Property Analysis

The Wudong colliery in the Urumchi coal field served as the study area. The Urumchi coal field is located in northern part of Tianshan Mountain, and there are 33 available coal-bearing strata there from the Xishanyao group of the Jurassic Period (Figure 1). The total thickness of the coal seams in the study area was 50 m, and the angle ranged from 65° to 87°, with an average angle of about 86°. Table 1 introduces the roof and floor values of the seams in B_{3-6}. Figure 2 shows the thicknesses and spans of the seams from B_3 to B_6. Thereafter, there were many interbeds in B_{4-5}, and their thicknesses were between 0.15 and 0.20 m. The petrographic compositions of B_{3-6} are also shown in Table 1. Over 95% of maceral composition of the coal are Vitrinite and Inertinite, so microlithotype of the coal is vitrinertite. On account of the vitrinertite and some pyrite being associated with the coal seams, the coal has a short spontaneous combustion cycle in the study area. However, both coal dust and methane pose low explosive hazards.

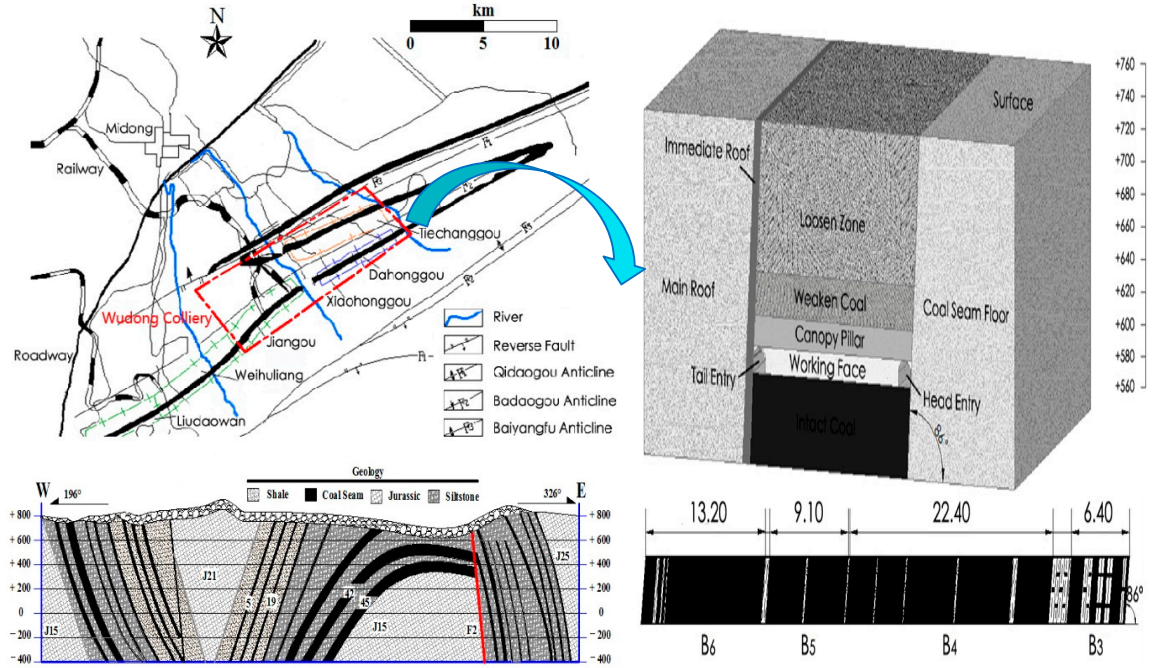

Figure 1. Profiles of the study area including the simplified geological conditions, sectional map with main lithostratigraphic units, and the coal excavation settings.

Table 1. Introductions to petrographic composition and roof and floor of B_{3-6} of study area.

Name	Lithology	Thickness (m)	Description
Main Roof	Shale	1.90	hard, dark grey, and lamellar
Immediate Roof	Siltstones	0.70	Lamellar and joint obviously
False Roof	Shale	0.10	Soft and joint obviously
Coal Seam Floor	Shale	0.55	Joint and fragile

Serial number	Maceral composition(%)					
	Vitrinite	Average	Inertinite	Average	Liptinite	Average
B_{3-6}	33.50–62.60	46.60	37.40–65.60	52.80	0.00–1.90	0.60
	Organic matter(%)	Inorganic matter(%)		Vitrinite reflectance(%)		Microlithotype
	86.35	13.65		0.67		vitrinertite

All the presented coal and rock samples in this paper were collected from the southern lane of the Wudong coal mine in the Urumchi coal field, specifically the top coal caving face at the No. 45 coal seam at the +500 m level. The KJ743 coal mine geostress monitoring system was used to collect

real-time stress data. Figure 2a presents a plot of the stress data from November 11, 2014 to February 2, 2015. The vertical geostress remained fairly constant with small fluctuations within a narrow range due to the excavation disturbances in the area. The value of the vertical geostress varied from 6.8 MPa to 7.0 MPa. The distributions of the maximum and minimum principal horizontal stress are presented in Figure 2b,c. In particular, the minimum principal horizontal stress varied from 7.6 MPa to 8.4 MPa. From 340 m to 400 m, the minimum principal horizontal stress increased slightly due to a disturbance caused by the excavation activities. The maximum principal horizontal stress exhibited a uniform distribution. The maximum principal horizontal stress remained constant at 10.0 MPa, except locally at 480 m and 250 m, where it increased to 13.0 MPa and 28.8 MPa, respectively.

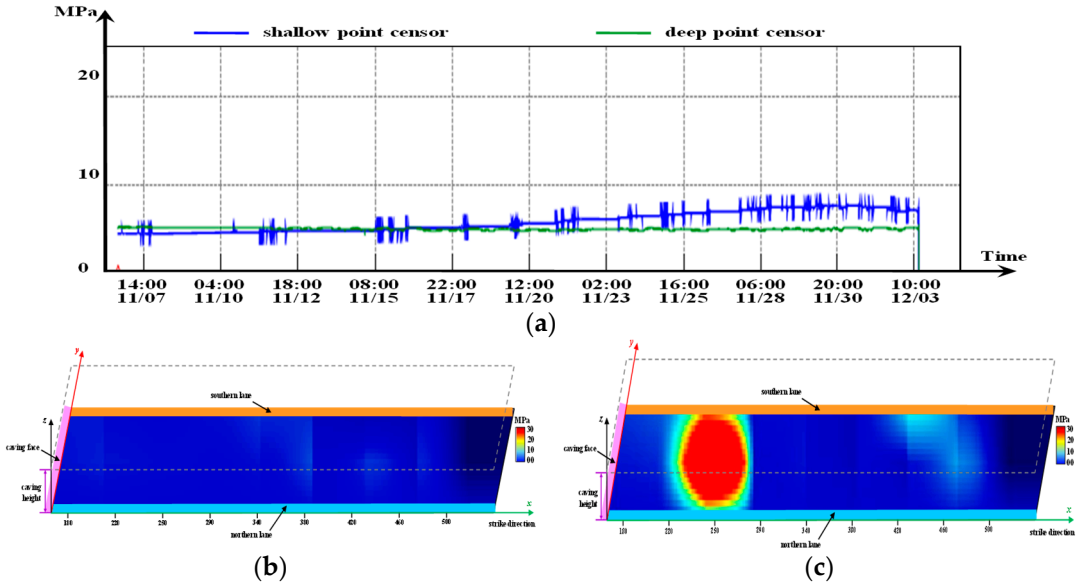

Figure 2. Results of the in-situ monitoring of the regional geostress: (**a**) vertical geostress; (**b**) minimum principal horizontal stress; (**c**) maximum principal horizontal stress.

Both the axial and radial stresses of the coal were zero following in-situ sampling. Following sampling, the samples were immediately returned to the Laboratory of Western Mines and Hazard Prevention, Ministry of Education of China for preparation with the plastic package. The rock was composed of siltstone with a small quantity of mudstone and argillaceous sandstone. The rock exhibited a relatively uniform particle size that varied from 0.30 to 0.90 mm with an average particle size of 0.70 mm. The fracture of the coal was like fine granulated sugar. The coal sample surface was fresh with a few apparent protogenetic cracks. The coal sample was prepared in strict accordance with the IRTM method recommended by the International Society for Rock Mechanics (ISRM) and the samples were cubes with side lengths equal to 60 mm following cutting in triplicate [22]. The surface was carefully ground without remarkable flaws. Moreover, both the nonparallelism and non-perpendicularity errors were less than 0.05 mm. Figure 3 presents the quartile statistical results of geometric dimensioning in the three orientations of the coal. Although a slightly discrepancy was observed in the finished sizes, the mean value of error did not exceed 1.0 mm.

In the AE test, seven coal and rock samples were employed, and the serial numbers of the samples were respectively from LXMT-01 to LXMT-07 for the coal samples and from LXYT-01 to LXYT-07 for the rock samples. The variable coefficients of all the parameters were within 5%, thereby indicating that the physical properties of the samples were well-consistent and validating the applicability of the samples in the follow-up experiments (refer to the Appendix A).

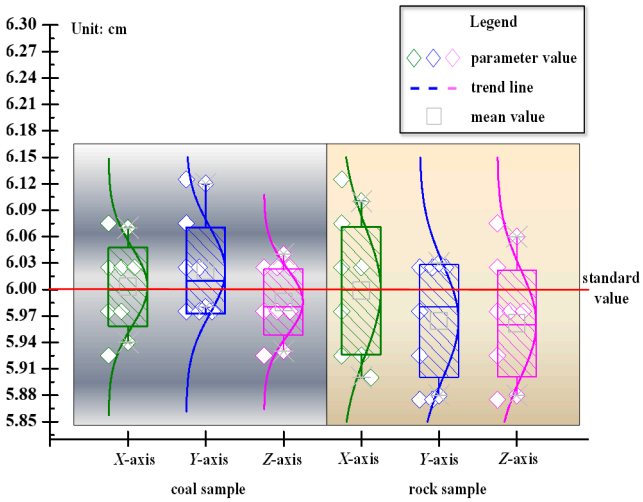

Figure 3. Stochastic statistics of the geometric dimension quartile of coal and rock samples.

2.2. Experimental Facility and Monitoring Technique

Figure 4 shows the AE testing scheme of coal and rock fracturing with uniaxial compression. The WE-10 rock mechanics testing machine was used in the experiment for both the AE and energy dissipation regularities during the coal fracturing process. The loading mode was the displacement control at a loading velocity of 0.1 mm/min, which complied with a series of ISRM experimental procedures. The prepared samples with the No. 40Cr alloy steel rigid cushions had a side length of 70 mm and a thickness of 10 mm. The top and bottom were placed in the testing machine. In the axial orientation, the sample was loaded until it exhibited failure due to axial unloading. The real-time loading values and the corresponding axial deformation were automatically acquired from the testing machine. This paper offers an SDAES7.5 AE instrument to record the acoustic wave energy in various stages during sample fracturing. All the energy data was applied to characterize the energy dissipation and liberation mechanism of the coal. The AE sensor was coupled with the sample using Vaseline. To minimize the interference of the external acoustic sources, the AE parameters were determined after adjusting the threshold value several times. In the experiment, real-time AE monitoring was employed to monitor synchronization with the external loading.

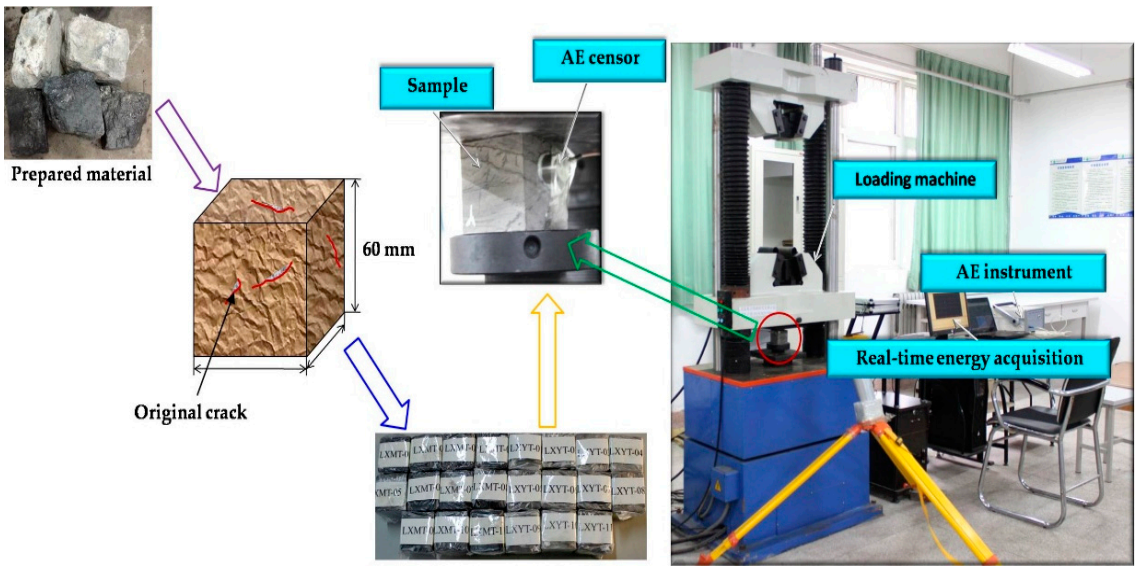

Figure 4. The acoustic emission testing scheme of coal and rock fracturing with uniaxial compression.

3. Coal Fracturing Mechanism

The characteristics of progressive failure were obvious with typical nonlinear deformation characteristics, especially the rock sample [23–27]. The basic mechanical parameters of all the samples are presented in Table 2. Here, σ_p and σ_r represent the peak and residual strengths, respectively. ε_p represents the strain value corresponding to the peak strength. E_t and E_b represent the elastic and deformation moduli, respectively. In particular, E_t is the average slope of the approximate linear part in the curves. In addition, E_b represents the stress-strain ratio at the point where the stress value was 50% that of the peak strength. All the presented strain values are the means of the experimental values. According to the Appendix A, the basic mechanical parameters exhibited large discreteness values due to a significant difference in the internal sample structures of the various sampling positions.

Table 2. Profile of the mechanical parameters and discreteness of the unloading coals.

Sample Serial Number	σ_p (MPa)	σ_r (MPa)	ε_p (10^{-3})	E_t (MPa)	E_b (MPa)	dε/dt (10^{-3}/s)
LXMT-01	18.57	11.53	98.30	595	110	
LXMT-02	14.37	7.55	85.75	956	91	
LXMT-03	12.45	6.44	69.60	410	122	
LXMT-04	11.74	6.11	52.62	660	142	0.56
LXMT-05	9.72	4.91	78.47	518	73	
LXMT-06	17.26	8.87	68.20	682	148	
LXMT-07	17.99	12.61	96.42	780	109	
LXYT-01	25.36	12.52	72.30	877	231	
LXYT-02	15.48	9.94	70.40	727	128	
LXYT-03	19.05	13.68	39.96	590	330	
LXYT-04	12.43	10.81	40.08	440	259	0.55
LXYT-05	37.26	18.48	34.41	764	668	
LXYT-06	43.13	24.97	54.83	716	525	
LXYT-07	39.03	19.87	52.50	689	622	
Lithology	Discrete parameter	σ_p	σ_r	ε_p	E_t	E_b
Coal	$\overline{X}$	**14.59**	**8.29**	**78.48**	**657**	**114**
	E	3.44	2.88	16.44	178	27
	ζ	23.578	34.741	20.948	27.093	23.684
Rock	$\overline{X}$	**27.39**	**15.75**	**52.07**	**686**	**395**
	E	12.38	5.51	15.03	138	210
	ζ	45.199	34.984	28.865	20.117	53.165

As compared to normal isotropic materials, the internal structure of the coal and rock was divided into multiple structural units (MSU) by a few main cracks, which significantly affected the sample strength. The stress-strain curves exhibited a smooth monotonic increase at the onset of the AE test. The loading value of each MSU during the AE test ceaselessly exceeded its failure strength limit following an increase in the external loading. Therefore, essential differences were observed in the mechanical response characteristics and deformation characteristics of the coal and rock as compared to those of other materials. When the curves exhibited a smooth monotonic increase, the main cracks in both the coal and rock samples started to close due to the influence of external loading. Following a continuous increase in the external loading, the MSU with minimum of failure strength limit presented a yielding state, thereby generating a rapid decrease in the bearing capacity of the MSU until the bearing capacity was equal to zero, which was the threshold of the nonlinear constitutive relationship of the coal and rock.

A further increase in the axial loading resulted in the persistent destruction of the other MSU. The failure of samples was presented as progressive failure. When the external loading exceeded the maximum bearing capacity, the samples exhibited macroscopic fracturing and destabilization. We defined the MSU with a maximum bearing capacity as the primary MSU, of which the primary MSU exhibited the greatest influence on the characteristics of the coal and rock fracturing. Moreover,

the bearing capacity of the primary MSU was equal to the peak strength in the stress-strain curve. Following the destruction of the primary MSU, the axial stress level of the samples kept decreasing and the MSU with minimum bearing capacity initially exhibited an integral yield. The other MSU then started to release without yielding phenomena. In conclusion, the post peak-point exhibited a weakened yield in the local area of the coal and rock, which were defined as the local distortion characteristics of the coal and rock. Therefore, the strain value after the peak point should only consider the plastic strain of the local yielding weakening region.

The yield, damage, and failure of the coal and rock essentially exhibited energy dissipation and liberation [28–30]. The energy being dissipated with the sample failure, U, may be defined as the work done to the coal by the mechanical testing machines under continuous axial loading condition, as defined by Equation (1) as follows:

$$U = \int Fdu = SL \int \sigma d\varepsilon = L^3 \Psi = V\Psi \quad (1)$$

where L, S, and V represent the side length, bottom area, and volume, respectively; and Ψ represents the dissipated energy per unit volume of the samples, where Ψ is equal to the corresponding area of the stress-strain curve and has a unit of MJ/m^3. Figure 5 presents the quantitative relation of the AE event parameters between the axial stress and time sequence. The whole AE test was categorized into four stages based on both the axial stress and AE event parameters:

(1) Initial loading stage (I). The stress-time curve exhibited a horizontal trend at the stage, and dU/dt, wherein the gaining rate of dissipated energy exhibited an obvious increase. The internal original cracks began to close under the loading condition and the mechanical characteristics tended to exhibit a quasi-isotropic status. The coal and rock samples exhibited stage durations of 25–30 s and 10–18 s, because the internal structure of the rock sample was simpler with fewer cracks and a structural plane. The AE counting number was smallest in all the stages and the Kaiser point of the partial coal samples was observed at this stage.

(2) Elastic stage (II). The samples were regarded as elastic medium at the beginning, and the σ-t curve exhibited an approximately linear trend at this stage. dU/dt was maintained steady on the whole. The coal and rock samples exhibited roughly similar stage durations of 25 s and 20 s, respectively. The samples started to transform from an elastomeric to elastic-plastic material following a gradual increase in the axial loading. Some partial mutations were observed in the σ-t curve, especially the curve of the rock sample. The possible sudden instability of the main crack in the rock may have generated overall structural distortion. In addition, the AE counting number increased in each subsequent stage and most of the samples exhibited the Kaiser point during the elastic stage.

(3) Micro-fracturing stage (III). The samples were regarded as plastic media and the σ-t curve exhibited a concave shape with a greater slope. However, dU/dt exhibited an initial decrease in the micro-fracturing stage following an increase in the time sequence. This stage exhibited the longest duration, and the coal and rock samples exhibited durations of about 70 s and 30 s, respectively. The loading resistance of the coal sample to the axial loading was poor as compared to the rock sample and the axial loading was proportional to the time sequence. In addition, dU/dt was maintained steady. Due to the specific structural characteristics of the rock, the primary MSU played a dominating role in resisting the axial loading. In addition, the progressive failure was observed in the rock σ-t curve. Before and after the arrival of the peak point, the curve exhibited dentate fluctuation because the secondary MSU opposed the axial loading. The AE counting number increased sharply near the peak point and presented the maximum AE counting number.

(4) Post-peak fracturing stage (IV). The structures of the samples were completely destroyed. The σ-t curve dropped suddenly and then exhibited persistent fluctuation near the peak point. On behalf of the more intact structure of the rock sample, the residual stress of the rock sample was so large that the rock sample easily opposed the external loading. An obvious reduction in dU/dt was observed at the peak point. A shorter duration of approximately 15–25 s was observed. Large-scale

mesoscopic deformation and macroscopic fracturing was observed within a short time, and the AE counting number was observed in the last increment at a lower increment rate.

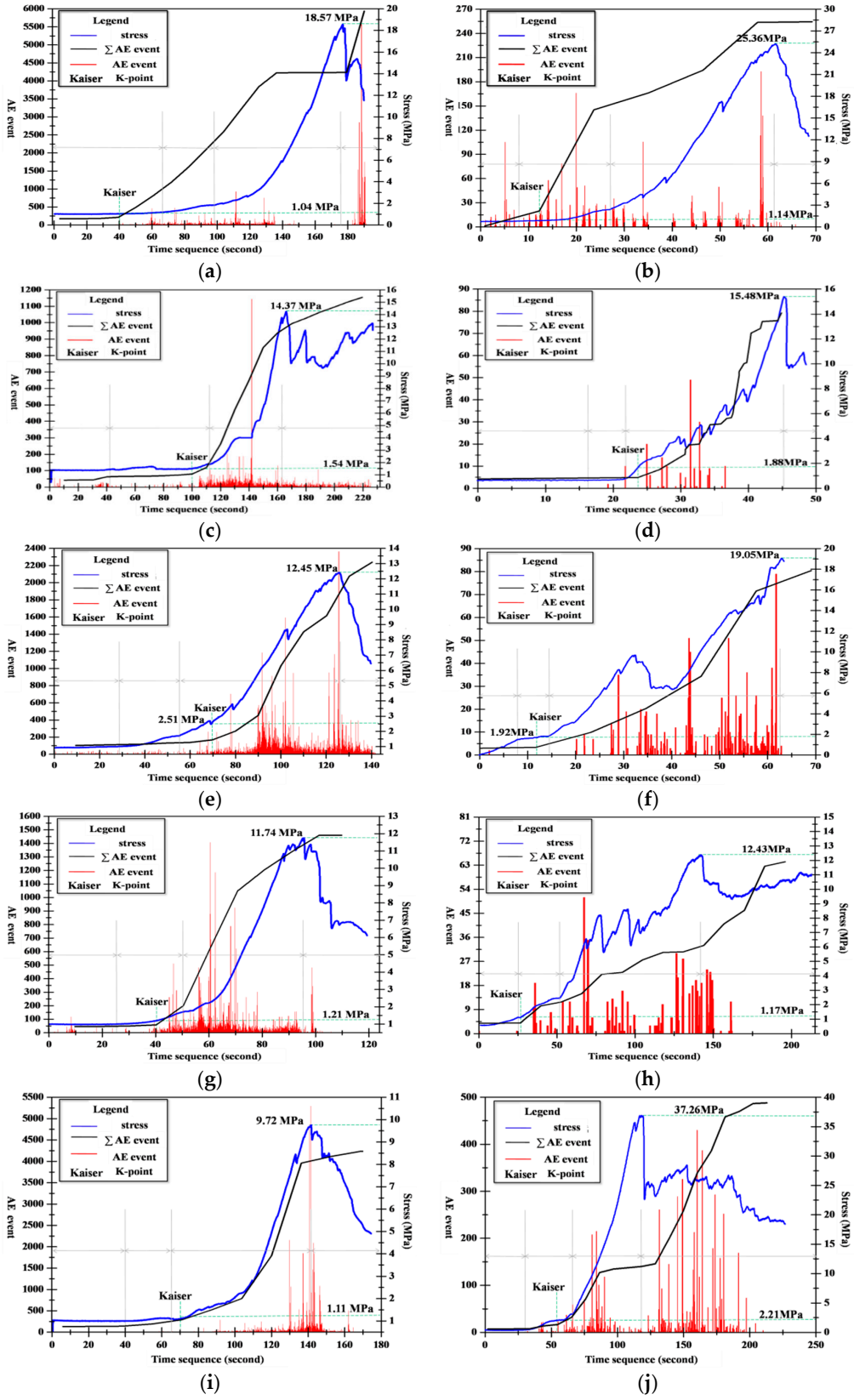

Figure 5. *Cont.*

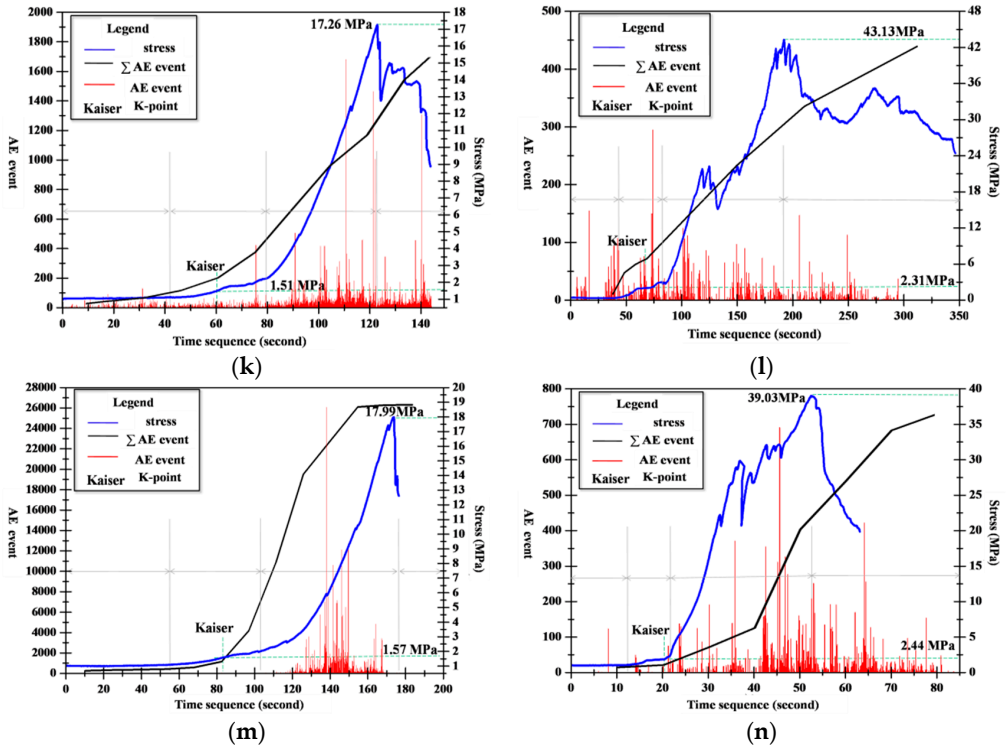

Figure 5. Plot for the time-based relation of the parameters, including the axial stress, AE counting number, and total counting number of coals: (**a**) LXMT-01; (**b**) LXYT-01; (**c**) LXMT-02; (**d**) LXYT-02; (**e**) LXMT-03; (**f**) LXYT-03; (**g**) LXMT-04; (**h**) LXYT-04; (**i**) LXMT-05; (**j**) LXYT-05; (**k**) LXMT-06; (**l**) LXYT-06; (**m**) LXMT-07; and (**n**) LXYT-07.

4. Analytical Discussion

Table 3 lists all the energy parameter data, including U, Ψ, K_t, and E_{AE}, wherein K_t represents the accumulated elastic strain energies when the axial stress was equal to the peak value, and K_t is equal to ${\sigma_p}^2/2E_t$. Here, E_t is defined as the elasticity modulus of the samples based on the description of the sample deformation trait. As an important mechanical index, K_t was usually provided to assess the dynamic failure events caused by underground coal excavation. Furthermore, E_{AE} represents the acoustic wave energy. According to analysis of the energy data in Table 2, the quantitative correlation between Ψ and $E_{AE\text{-}II}/\Sigma E_{AE}$ is defined as follows:

$$\Psi = K_t e^{a+\frac{\frac{E_{AE-II}}{\sum E_{AE}}}{b}} \tag{2}$$

where ΣE_{AE} defines the accumulated energy of the acoustic waves from the samples by AE (J); $E_{AE\text{-}II}$ is the accumulated energy of the acoustic waves in the elastic stage (J); and $E_{AE\text{-}II}/\Sigma E_{AE}$ defines the percentage of the two above energy parameters ratios. In addition, a and b are both material parameters. Equation (2) was compiled as Equation (3). By means of the least square method, a linear relation between $\ln(\Psi/K_t)$ and $E_{AE\text{-}II}/\Sigma E_{AE}$ was established to define the material parameters.

$$\ln\frac{\Psi}{K_t} = a + \frac{\frac{E_{AE-II}}{\sum E_{AE}}}{b} \tag{3}$$

Table 3. Energy parameters of the coal-rock samples in continuous axial compressed testing.

Lithology	Sample Number	σ_{Kaiser} (MPa)	Ψ (MJ/m^3)	U (J)	K_t (MJ/m^3)	Ψ/K_t	ΣE_{AE} (J)	AE Stage	E_{AE} (J)	$E_{AE\text{-}II}/\Sigma E_{AE}$ (%)
Coal sample	LXMT-01	1.04	0.491	106.41	0.290	1.445	0.477	I	0.014	2.94
								II	**0.022**	**4.64**
								III	0.330	69.15
								IV	0.111	23.27
	LXMT-02	2.51	0.331	73.05	0.108	3.067	0.101	I	0.001	0.99
								II	**0.007**	**6.95**
								III	0.073	72.26
								IV	0.020	19.80
	LXMT-03	1.54	0.356	77.15	0.189	1.883	0.514	I	0.001	0.19
								II	**0.033**	**6.52**
								III	0.299	58.27
								IV	0.180	35.02
	LXMT-04	1.21	0.285	60.44	0.104	2.740	0.172	I	0.001	0.58
								II	**0.013**	**7.83**
								III	0.156	90.42
								IV	0.002	1.17
	LXMT-05	1.11	0.324	70.45	0.182	1.779	0.546	I	0.012	2.20
								II	**0.039**	**7.08**
								III	0.461	84.49
								IV	0.034	6.23
	LXMT-06	1.51	0.418	91.80	0.218	1.916	0.552	I	0.012	2.17
								II	**0.031**	**5.59**
								III	0.391	70.83
								IV	0.118	21.41
	LXMT-07	1.42	0.479	101.24	0.207	2.375	0.499	I	0.018	3.61
								II	**0.024**	**4.81**
								III	0.429	85.97
								IV	0.028	5.61
Rock sample	LXYT-01	1.14	2.066	446.31	0.367	1.98	0.293	I	0.007	2.39
								II	**0.078**	**26.55**
								III	0.206	70.37
								IV	0.002	0.69
	LXYT-02	1.88	1.917	419.41	0.165	4.158	0.215	I	0.002	0.93
								II	**0.059**	**27.57**
								III	0.142	66.38
								IV	0.011	5.12
	LXYT-03	1.92	1.848	397.22	0.308	2.165	0.240	I	0.001	0.42
								II	**0.067**	**28.07**
								III	0.157	66.09
								IV	0.013	5.42
	LXYT-04	1.17	1.551	321.19	0.176	3.237	0.114	I	0.001	0.88
								II	**0.035**	**30.48**
								III	0.070	61.63
								IV	0.008	7.01
	LXYT-05	2.21	3.904	820.87	0.455	2.364	0.242	I	0.001	0.41
								II	**0.043**	**17.83**
								III	0.109	44.98
								IV	0.089	36.78
	LXYT-06	2.31	3.537	783.21	0.650	1.570	0.384	I	0.006	1.57
								II	**0.074**	**19.18**
								III	0.238	62.07
								IV	0.066	17.18
	LXYT-07	2.44	3.662	801.47	0.557	1.866	0.194	I	0.001	0.52
								II	**0.036**	**18.71**
								III	0.076	39.02
								IV	0.081	41.75

Each point ($\ln(\Psi/K_t)$, $E_{AE\text{-}II}/\Sigma E_{AE}$) was drawn in the coordinate system and observed using the relevant fitted curve. All the points exhibited a near-linear line, thereby allowing the adoption of the linear function. The square difference (χ) between the measured (Y_i) and calculated values (Y_j) fulfilled the optimization criterion following the application of the least square method. Supposing a_0 is equal to $1/b$, Equation (3) can be substituted into the optimization criterion as Equation (4).

$$\chi = \sum_{i=1}^{n}\left(Y_i - Y_j\right)^2 = \sum_{i=1}^{n}\left\{\left(\ln\frac{\Psi}{K_t}\right)_i - \left[a + a_0\left(\frac{E_{AE-II}}{\sum E_{AE}}\right)_i\right]\right\}^2 \tag{4}$$

Equation (4) exhibits the minimum, such that the partial derivatives of χ to both a and a_0 are equal to zero, as presented in Equations (5) and (6).

$$\frac{\partial\chi}{\partial a} = \sum_{i=1}^{n}\left[a + a_0\left(\frac{E_{AE-II}}{\sum E_{AE}}\right)_i - \left(\ln\frac{\Psi}{K_t}\right)_i\right] = 0 \tag{5}$$

$$\frac{\partial\chi}{\partial a_0} = \sum_{i=1}^{n}\left(\frac{E_{AE-II}}{\sum E_{AE}}\right)_i\left[a + a_0\left(\frac{E_{AE-II}}{\sum E_{AE}}\right)_i - \left(\ln\frac{\Psi}{K_t}\right)_i\right] = 0 \tag{6}$$

The following equations define an equation set for a and a_0,

$$na + \left[\sum_{i=1}^{n}\left(\frac{E_{AE-II}}{\Sigma E_{AE}}\right)_i\right]a_0 = \sum_{i=1}^{n}\left(\ln\frac{\Psi}{K_t}\right)_i \tag{7}$$

$$\left[\sum_{i=1}^{n}\left(\frac{E_{AE-II}}{\Sigma E_{AE}}\right)_i\right]a + \left[\sum_{i=1}^{n}\left(\frac{E_{AE-II}}{\Sigma E_{AE}}\right)_i\right]^2 a_0 = \sum_{i=1}^{n}\left[\left(\frac{E_{AE-II}}{\Sigma E_{AE}}\right)_i\left(\ln\frac{\Psi}{K_t}\right)_i\right] \tag{8}$$

where n is equal to 7. The equation solutions are as follows:

$$a = \sum_{i=1}^{7}\left(\ln\frac{\Psi}{K_t}\right)_i/7 - a_0\left[\sum_{i=1}^{7}\left(\frac{E_{AE-II}}{\Sigma E_{AE}}\right)_i\right]/7 \tag{9}$$

$$a_0 = 7\sum_{i=1}^{7}\left[\left(\frac{E_{AE-II}}{\Sigma E_{AE}}\right)_i\left(\ln\frac{\Psi}{K_t}\right)_i\right] - \sum_{i=1}^{7}\left[\left(\frac{E_{AE-II}}{\Sigma E_{AE}}\right)_i\left(\ln\frac{\Psi}{K_t}\right)_i\right]/\left\{7\left[\sum_{i=1}^{7}\left(\frac{E_{AE-II}}{\Sigma E_{AE}}\right)_i^2\right] - \left[\sum_{i=1}^{7}\left(\frac{E_{AE-II}}{\Sigma E_{AE}}\right)\right]^2\right\} \tag{10}$$

The data from Table 3 were inserted into Equations (9) and (10) to obtain the material parameter solutions shown in Table 4. In addition, the relationship between $\ln(\Psi/K_t)$ and $E_{AE\text{-}II}/\Sigma E_{AE}$ for the coal and rock samples was defined as follows:

$$\begin{cases} \Psi_{\text{coal-sample}} = 0.162e^{1.903-0.171\frac{E_{AE-II}}{\Sigma E_{AE}}} & (R\approx 1.051) \\ \Psi_{\text{rock-sample}} = 0.547e^{3.267-0.073\frac{E_{AE-II}}{\Sigma E_{AE}}} & (R\approx 0.949) \end{cases} \tag{11}$$

Table 4. Values of the material parameters during coal and rock sample fracturing.

Parameter	a	a_0	$1/b$	K_t
Coal sample	1.903	−5.841	−0.171	0.162
Rock sample	3.267	−13.636	−0.073	0.547

Both sides of Equation (2) were multiplied with the volume (L^3). Equation (12) defines the theoretical model on the dissipation energy during sample fracturing based on AE event energy parameters.

$$U = L^3 K_t e^{a+\frac{\frac{E_{AE-II}}{\sum E_{AE}}}{b}} \tag{12}$$

The coal and rock samples exhibited minimum (maximum) values of U of 60.44 J (106.41 J) and 321.19 J (820.87 J), respectively. Supposing U/L^3K_t=Y and $\Sigma E_{AE\text{-}II}/\Sigma E_{AE}$=$X$, Equation (12) can be changed altered as Equation (13).

$$Y = e^{a+\frac{1}{b}X} \tag{13}$$

The derivative of both sides with respect to X was taken for Equation (13), and the result is defined in Equation (14).

$$\frac{\mathrm{d}Y}{\mathrm{d}X} = \frac{e^{a+\frac{1}{b}X}}{b} \tag{14}$$

where $\mathrm{d}Y/\mathrm{d}X$ must be less than zero to allow Equation (13) to be defined as a monotone descending function, thereby indicating that a decrease in U generates an increase in $\Sigma E_{AE\text{-}II}/\Sigma E_{AE}$. In the elastic stage, the dissipation energy was much lower that the work done by the testing machine was used for crack initiation and propagation. When the anisotropy of the samples was further increased, the deformation and fracturing velocity of the samples accelerated due to external loading. In both the micro-fracturing and post-peak fracturing stages, much of the work done by the testing machine transformed into more acoustic waves that were received by the AE instrument. Moreover, the other work was dissipated by the macroscopic cracks and the structure friction.

5. Conclusions

(1) The relevant mechanical parameter discreteness was too large because the internal structure of the coal and rock was divided into multiple structural units (MSUs) due to the presence of a few main cracks. The MSU with the maximum bearing capacity was defined as the primary MSU, and the maximum bearing capacity was equal to the peak strength of the stress-strain curve. The post peak-point exhibited yielding weakening in the local area of the coal and rock, which defined the local distortion characteristics of the coal and rock. The strain value after the peak point should only consider the plastic strain of the local yielding weakening region.

(2) The entire acoustic emissions (AE) test was categorized into four stages based on both the axial stress and AE event parameters: initial loading, elastic, micro-fracturing, and post-peak fracturing stages. The coal and rock samples exhibited minimum (maximum) values of U of 60.44 J (106.41 J) and 321.19 J (820.87 J), respectively.

(3) A theoretical model on the dissipation energy during sample fracturing based on AE event energy parameters was offered. A decrease in U was observed following an increase in $\Sigma E_{AE\text{-}II}/\Sigma E_{AE}$.

Author Contributions: S.P. proposed the innovative points and conceived the study. S.P. and L.X. (Xiaoming Liu) wrote the paper. L.X. (Xingping Lai) revised the paper.

Acknowledgments: Financial support for this work was provided by the 973 Key National Basic Research Program of China (No. 2015CB251602), the Natural Science Foundation of Shaanxi Province (No. 2018JQ5194), the China Postdoctoral Science Foundation (No. 2017M623328XB), the Science and Technology Innovation Team Project of Shaanxi Province (No. 2018TD-038), the Hunan Province Engineering Research Center of Radioactive Control Technology in Uranium Mining and Metallurgy & Hunan Province Engineering Technology Research Center of Uranium Tailings Treatment Technology (No. 2018YKZX2001), and the Opening Project of Cooperative Innovation Center for Nuclear Fuel Cycle Technology and Equipment, University of South China (No. 2019KFY25). Support from these agencies is gratefully acknowledged.

Conflicts of Interest: The authors declare no conflict of interest.

Appendix A

In the AE testing, Table below presents the specific conditions of the physical propertiesAE tests, including the sample mass, sample dimension, and surface appearance. Equations (A1)–(A3) can be used to analyze the discreteness of all the physical parameter, of which the corresponding calculation results are listed in Table A1.

$$\overline{X} = \frac{1}{n}\sum_{i=1}^{n} X_i \tag{A1}$$

$$E = \sqrt{\frac{1}{n-1}\sum_{i=1}^{n} (X_i - \overline{X})^2} \tag{A2}$$

$$\zeta = \frac{E}{\overline{X}} \times 100\% \tag{A3}$$

where $\overline{X}$ is the mean value, E is the standard difference, and ζ is the variable coefficient.

Table A1. Profile of the basic physical parameters and discreteness of coal and rock.

Sample Number	Mass(g)	Geometric Dimension (mm)			Volume (cm^3)	Density (g/cm^{-3})	Appearance Description
		X-axis	*Y*-axis	*Z*-axis			
LXMT-01	283	59.9	60.1	60.2	216.719	1.306	Apparent through cracks in *Y*-axis
LXMT-02	291	60.3	61.2	59.8	220.684	1.319	Apparent through cracks in all axes
LXMT-03	283	60.0	60.5	59.7	216.711	1.306	Apparent tiny cracks in all axes
LXMT-04	278	59.4	59.9	59.6	212.060	1.311	Apparent through cracks in *Y*-axis
LXMT-05	288	60.3	60.1	60.0	217.442	1.324	Apparent cracks in both *X*- and *Z*-axes
LXMT-06	289	60.7	59.9	60.4	219.610	1.316	Apparent tiny cracks in all axes
LXMT-07	275	59.6	59.8	59.3	211.350	1.301	Apparent tiny cracks in all axes
LXYT-01	580	59.9	60.3	59.8	215.996	2.685	Whole is more complete with small surface cracks
LXYT-02	540	59.2	59.8	61.8	218.782	2.638	Whole is more complete with small surface cracks
LXYT-03	573	60.0	60.2	59.5	214.914	2.666	Clear grain, through cracks in *X*,*Y*- and *Y*,*Z*-axis
LXYT-04	549	59.0	58.9	59.6	207.116	2.651	Clear grain, through cracks in *X*,*Y*- and *Y*,*Z*-axis
LXYT-05	561	60.1	59.3	59.0	210.272	2.668	Whole is more complete with small surface cracks
LXYT-06	594	60.7	60.2	60.6	221.441	2.682	Clear grain, through cracks in *X*,*Y*- and *Y*,*Z*-axis
LXYT-07	592	61.0	59.8	60.0	218.868	2.705	Apparent cracks in both *X*- and *Z*-axes

Lithology	Discrete parameter	L_X (mm)	L_Y (mm)	L_Z (mm)	Mass (g)	Density (g/cm^{-3})
Coal mass	$\overline{X}$	60.0	60.2	59.5	284	1.312
	E	0.447	0.491	0.537	5.902	0.008
	ζ	0.745	0.816	0.903	2.078	0.610
Rock	$\overline{X}$	60.0	59.6	59.6	570	2.671
	E	0.725	0.642	0.607	20.781	0.0223
	ζ	1.208	1.077	1.018	3.646	0.835

References

1. Lai, X.P.; Shan, P.F.; Cao, J.T.; Cui, F.; Sun, H. Simulation of asymmetric destabilization of mine-void rock masses using a large 3D physical model. *Rock Mech. Rock Eng.* **2016**, *49*, 487–502. [CrossRef]
2. Lai, X.P.; Sun, H.; Shan, P.F.; Cai, M.; Cao, J.T.; Cui, F. Structure instability forcasting and analysis of giant-rock-pillars in steeply dipping thick coal seams. *Int. J. Miner. Metall. Mater.* **2015**, *22*, 1–12. [CrossRef]
3. Sun, H.; Liu, X.L.; Zhu, J.B. Correlational fractal characterisation of stress and acoustic emission during coal and rock failure under multilevel dynamic loading. *Int. J. Rock Mech. Min. Sci.* **2019**, *117*, 1–10. [CrossRef]
4. Zhao, Y.S.; Feng, Z.C.; Wan, Z.J. Least energy principle of failure of rock. *Chin. J. Rock Mech. Eng.* **2003**, *22*, 1781–1783. (In Chinese)
5. Luo, Y.; Xie, H.P.; Ren, L.; Zhang, R.; Li, C.B.; Gao, C. Linear elastic fracture mechanics characterization of an anisotropic shale. *Sci. Rep.* **2018**, *8*, 8505. [CrossRef]
6. Jin, F.N.; Jiang, M.R.; Gao, X.L. Defining damage variable based on energy dissipation. *Chin. J. Rock Mech. Eng.* **2004**, *23*, 1976–1980. (In Chinese)

7. Hu, L.Q.; Li, X.B.; Zhao, F.J. Sudy on energy consumption in fracture and damage of rock induced by impact loadings. *Chin. J. Rock Mech. Eng.* **2003**, *21* (Suppl. 2), 2304–2308. (In Chinese)
8. Sun, Q.; Li, S.C.; Feng, X.D.; Li, W.T.; Yuan, C. Study of numerical simulation method of rock fracture based on strain energy density theory. *Rock Soil Mech.* **2011**, *32*, 1575–1582. (In Chinese)
9. Gong, W.L.; Peng, Y.Y.; Wang, H.; He, M.; e Sousa, L.R.; Wang, J. Fracture angle analysis of rock burst faulting planes based on true-triaxial experiment. *Rock Mech. Rock Eng.* **2015**, *48*, 1017–1039. [CrossRef]
10. Xu, Y.; Dai, F.; Xu, N.W.; Zhao, T. Numerical investigation of dynamic rock fracture toughness determination using a semi-circular bend specimen in split Hopkinson pressure bar testing. *Rock Mech. Rock Eng.* **2016**, *49*, 731–745. [CrossRef]
11. Stanchits, S.; Burghardt, J.; Surdi, A. Hydraulic fracturing of heterogeneous rock monitored by acoustic emission. *Rock Mech. Rock Eng.* **2015**, *48*, 2513–2517. [CrossRef]
12. Hamstad, M.A. Frequencies and amplitudes of AE signals in a plate as a function of source rise time. In Proceedings of the 29th European Conference on Acoustic Emission Testing, Vienna, Austria, 8–10 September 2010.
13. Zelenyak, A.M.; Hamstad, M.A.; Sause, M.G. Modeling of acoustic emission signal propagation in waveguides. *Sensors* **2015**, *15*, 11805–11822. [CrossRef] [PubMed]
14. Faisal Haider, M.; Giurgiutiu, V. Theoretical and numerical analysis of acoustic emission guided waves released during crack propagation. *J. Intell. Mater. Syst. Struct.* **2018**. [CrossRef]
15. Haider, M.F.; Giurgiutiu, V. Analysis of axis symmetric circular crested elastic wave generated during crack propagation in a plate: A Helmholtz potential technique. *Int. J. Solids Struct.* **2018**, *134*, 130–150. [CrossRef]
16. Wisner, B.; Kontsos, A. Investigation of particle fracture during fatigue of aluminum 2024. *Int. J. Fatigue* **2018**, *111*, 33–43. [CrossRef]
17. Zhuang, D.Y.; Tang, C.A.; Liang, Z.Z.; Ma, K.; Wang, S.Y.; Liang, J.Z. Effects of excavation unloading on the energy-release patterns and stability of underground water-sealed oil storage caverns. *Tunn. Undergr. Space Technol.* **2017**, *61*, 122–133. [CrossRef]
18. He, M.C.; Zhao, F.; Cai, M.; Du, S. A novel experimental technique to simulate pillar burst in laboratory. *Rock Mech. Rock Eng.* **2015**, *48*, 1833–1848. [CrossRef]
19. Xiao, Y.X.; Feng, X.T.; Li, S.J.; Li, S.J.; Feng, G.L.; Yu, Y. Rock mass failure mechanisms during the evolution process of rock bursts in tunnels. *Int. J. Rock Mech. Min. Sci.* **2016**, *83*, 174–181. [CrossRef]
20. Ji, H.G.; Wang, H.W.; Cao, S.; Hou, Z.; Jin, Y. Experimental research on frequency characteristics of acoustic emission signals under uniaxial compression of granite. *Chin. J. Rock Mech. Eng.* **2012**, *31* (Suppl. 1), 2900–2905. (In Chinese)
21. Zhao, X.D.; Tang, C.A.; Li, Y.H.; Yuan, R.F.; Zhang, J.Y. Study of AE activity characteristics under uniaxial compression loading. *Chin. J. Rock Mech. Eng.* **2006**, *25* (Suppl. 2), 3673–3678. (In Chinese)
22. Hudson, J.A.; Crouch, S.; Fairhurst, C.E. stiff and servo-controlled testing machines. *Int. J. Rock Mech. Min. Sci.* **1999**, *36*, 279–289.
23. Shan, P.F.; Lai, X.P. Numerical simulation of the samples in the fluid-solid coupling process during the failure of a fractured coal based on the regional geostress characteristics. *Transp. Porous Media* **2018**, *124*, 1061–1079. [CrossRef]
24. Wang, M.; Liu, L.; Zhang, X.Y.; Chen, L.; Wang, S.Q.; Jia, Y.H. Experimental and numerical investigations of heat transfer and phase change characteristics of cemented paste backfill with PCM. *Appl. Eng.* **2019**, *150*, 121–131. [CrossRef]
25. Liu, L.; Zhu, C.; Qi, C.C.; Zhang, B.; Song, K.-I. A microstructural hydration model for cemented paste backfill considering internal sulfate attacks. *Constr. Build. Mater.* **2019**, *211*, 99–108. [CrossRef]
26. Liu, L.; Yang, P.; Qi, C.C.; Zhang, B.; Guo, L.J.; Song, K.-I. An experimental study on the early-age hydration kinetics of cemented paste backfill. *Constr. Build. Mater.* **2019**, *212*, 283–294. [CrossRef]
27. Huan, C.; Wang, F.H.; Li, S.T.; Zhao, Y.J.; Liu, L.; Wang, Z.H.; Ji, C.F. A performance comparison of serial and parallel solar-assisted heat pump heating systems in Xi'an, China. *Energy Sci. Eng.* **2019**. [CrossRef]
28. Shan, P.F.; Lai, X.P. Influence of CT scanning parameters on rock and soil images. *J. Vis. Commun. Image R.* **2019**, *58*, 642–650. [CrossRef]

29. Shan, P.F.; Lai, X.P. Mesoscopic structure PFC similar to 2D model of soil rock mixture based on digital image. *J. Vis. Commun. Image R.* **2019**, *58*, 407–415. [CrossRef]
30. Shan, P.F. Image segmentation method based on K-mean algorithm. *EUR. J. Image Video Proc.* **2018**. [CrossRef]